

Observational Signatures of High-Energy Emission during the Shallow Decay Phase of GRB X-Ray Afterglows

Y. W. Yu^{1,3}, X. W. Liu^{2,4}, and Z. G. Dai¹

¹*Department of Astronomy, Nanjing University, Nanjing 210093, China;
yuyw@nju.edu.cn, dzg@nju.edu.cn*

²*Purple Mountain Observatory, Chinese Academy of Sciences, Nanjing 210008, China;
xwliu@pmo.ac.cn*

³*Institute of Astrophysics, Huazhong Normal University, Wuhan 430079, China*

⁴*National Astronomical Observatories, Chinese Academy of Sciences, Beijing 100012, China*

ABSTRACT

The widely existing shallow decay phase of the X-ray afterglows of gamma-ray bursts (GRBs) is generally accepted to be due to long-lasting energy injection. The outflows carrying the injecting energy, based on their composition, could correspond to two types: baryon-dominated and lepton-dominated ones. The former-type outflows could be lagging materials in a wide GRB ejecta with a radial distribution of Lorentz factor, while the latter could be an electron-positron-pair wind that is driven by the post-burst central engine. We here provide a unified description for the dynamics of the two models of energy injection, and calculate the corresponding high-energy photon emission by considering the synchrotron radiation and inverse Compton scattering (including synchrotron self-Compton and combined inverse-Compton). We find that, for both models, there is a plateau (even a hump) in high-energy light curves during the X-ray shallow decay phase. In particular, a considerable fraction of the injecting energy in the leptonic-component-dominated model can be shared by the long-lasting reverse shock since it is relativistic. Furthermore, almost all of the energy of the reverse shock is carried by leptons and thus enhances the inverse-Compton emission dramatically. Therefore, this model predicts more significant high-energy afterglow emission than the baryonic-component-dominated model. We argue that these observational signatures would be used to discriminate between different energy-injection models in the upcoming *Gamma-ray Large Area Space Telescope* (GLAST) era.

Subject headings: gamma rays: bursts — radiation mechanism: nonthermal

1. Introduction

As discovered by Swift, there is a *shallow decay phase* (temporal indices $\alpha \sim [0, -0.8]$) from post-burst several tens of seconds to several hours (even days) occurring in the X-ray afterglow light curves of a significant fraction of gamma-ray bursts (GRBs) (Nousek et al. 2006; O’Brien et al. 2006; Willingale et al. 2007; Liang et al. 2007). This shallow decay phase is obviously beyond understanding of the standard afterglow model (Mészáros & Rees 1997; Sari et al. 1998), but it is generally accepted to be due to continuous energy injection into a relativistic blast wave (e.g., Zhang et al. 2006; Nousek et al. 2006; Fan & Xu 2006; Sollerman et al. 2007; de Pasquale et al. 2006, 2007; Liang et al. 2007). A simple injection luminosity, $\dot{E}_{\text{inj}} \propto t^{-q}$, is usually assumed in model fitting, although the specific nature of energy injection is not designated. Based on this assumption, Liang et al. (2007) recently found that the observed temporal and spectral indices during the shallow decay phase and subsequent normal decay phase are generally consistent with the injected closure relations with $q \sim 0$ and the closure relations of the standard afterglow models, respectively, thus suggesting that the shallow decay may result from roughly constant long-lived energy injection.

The physical nature of an injecting energy flow discussed in the literature involves two possible candidates: (i) lagging materials in a baryon-dominated GRB ejecta with a wide and radial distribution of Lorentz factor (Rees & Mészáros 1998; Panaitescu et al. 1998; Sari & Mészáros 2000; Granot & Kumar 2006; Liu et al. 2007), and (ii) a postburst energy flow originating from the central engine due to its long-lasting activity (Dai & Lu 1998a, 1998b; Zhang & Mészáros 2001a; Wang & Dai 2001; Dai 2004; Fan & Xu 2006; Yu & Dai 2007). In the former case, the energy deposited in the wide ejecta is released from the central engine during the prompt phase of the GRB, and feeds an outward-moving relativistic blast wave (i.e., the shocked medium) continuously during the afterglow phase. Because of an assumed power-law distribution of the Lorentz factor in the ejecta, the lagging lower-velocity materials catch up and collide with the foregoing higher-velocity but decelerated materials. This could lead to a long-lasting Newtonian or trans-relativistic reverse shock that propagates into the ejecta. Meanwhile, the heated ejecta pushes the blast wave and thus reduces the deceleration of the blast wave effectively, which accounts for the shallow decay. In the latter case, most of the energy that produces an afterglow is argued to be continuously released after (not during) the burst, but the GRB ejecta may provide only a relatively small amount of energy for the blast wave. Initially, the postburst energy flow may be dominated by electromagnetic waves (i.e., Poynting flux). However, as it propagates outward, the flow would evolve to an ultrarelativistic outflow dominated by a component of electron-positron pairs through some mechanisms (e.g., magnetic reconnection) at larger radii (Coroniti 1990; Michel 1994; Kirk & Skjæraasen 2003). It is this relativistic leptonic wind (not the electromagnetic flux) that

feeds the blast wave and produces a long-lasting relativistic reverse shock. The emission of the more and more energetic blast wave and the reverse shock gives rise to shallow decay. Therefore, we conclude from the above discussion that the postburst injecting energy flow is likely to be matter-dominated, which perhaps includes two types: a baryonic-component-dominated outflow and a leptonic-component-dominated outflow. The two corresponding representative models as described above are here called the radially structured ejecta (RSE) model (Rees & Mészáros 1998) and the relativistic wind bubble (RWB) model (Dai 2004), respectively.

In order to provide an effective test on the models mentioned above, a careful investigation of high-energy emission is important and urgent, as the launch and detection of GLAST are upcoming (Ritz 2007). In this paper, we calculate high-energy afterglow emission during the shallow decay phase of X-ray afterglows based on these two models and give corresponding observational signatures. Recently, Wei & Fan (2007), Fan et al. (2007), and Gou & Mészáros (2007) have made some attempts on high-energy afterglows. In their papers, the authors studied only the effect of the forward-shocked medium with the simple energy-injection form of $\dot{E}_{\text{inj}} \propto t^{-q}$, rather than considering the effect of the injecting flow itself. However, as found by Dai (2004), Uhm & Beloborodov (2007), Genet et al. (2007), Yu & Dai (2007), and Liu et al. (2007), the reverse shock that propagates into the injecting flow could play an important role in the emission in X-ray and/or optical bands in some situations. Therefore, high-energy emission features due to the reverse shock are also expected. In the RSE and RWB models, the high-energy photon emission from shocked materials is mainly produced by inverse Compton (IC) scattering between shock-accelerated electrons (for simplicity, electrons and positrons are not differentiated) and synchrotron seed photons (Sari & Esin 2001). Besides the synchrotron self-Compton (SSC) radiation of two shocked regions, we also consider two combined IC (CIC) processes, i.e., scattering of reverse shock photons by forward-shocked electrons and scattering of forward shock photons by reverse-shocked electrons, as pointed out by Wang, Dai & Lu (2001).

The structure of this paper is organized as follows: in the next section we provide a unified description for dynamics of the RSE and RWB models. In §3, we exhibit the energy distributions of shocked electrons that are determined by the shock-accelerating effect and the synchrotron & IC cooling effect, and formulate calculations of the synchrotron and IC radiation (including SSC and CIC). In §4, we show the numerical results of dynamics, spectra and light curves for some typical parameters in the two models. Finally, in §5, a summary is given and the observability of high-energy emission by the Large Area Telescope (LAT) instrument of GLAST is discussed.

2. Dynamics

As illustrated in Fig.1, in both RWB and RSE models, the system can be divided into four regions by the forward and reverse shocks¹: (1) the unshocked ambient medium, (2) the forward-shocked medium, (3) the reverse-shocked materials (i.e., shocked leptonic wind for the RWB model or shocked GRB ejecta for the RSE model), and (4) the unshocked cold wind or GRB ejecta, where regions 2 and 3 are separated by a contact discontinuity surface.

2.1. Structure of injecting flows

Figure 1 also shows illustrative Γ_i -distributions in all the regions. The main differences between the two models are the structure and composition of injecting flows:

(i) *The RWB model.* Following the analysis of Dai (2004) for a magnetar-driven wind, we simply assume that the leptonic wind propagates outward with a constant luminosity L_w and a constant bulk Lorentz factor Γ_w during a period of T_w after the burst². Thus, we can calculate the number density ($n_4^{(\text{RWB})}$) and the Lorentz factor ($\Gamma_4^{(\text{RWB})}$) of the pre-shock materials at the reverse shock front as

$$n_4^{(\text{RWB})} = n'_w(R) = \frac{L_w}{4\pi R^2 \Gamma_w^2 m_e c^3}, \quad (1)$$

$$\Gamma_4^{(\text{RWB})} = \Gamma_w, \quad (2)$$

where m_e is the rest mass of electrons and R is the radius of the system in the thin shell approximation.

¹It takes only a short time (tens to hundreds of seconds) for a reverse shock to cross the ejecta of a *typical* GRB in the RWB model. Two forward shocks forming initially during the interaction of the ejecta both with the medium and with the leptonic-component-dominated wind are assumed to merge to one forward shock simultaneously. In addition, the contribution of the GRB ejecta to the afterglow emission should be negligible as compared with the shocked medium and the shocked wind during the emission period of our interest. Thus, for simplicity, the structure of a RWB can be described approximately by Fig. 1(a). However, for the RSE model, the situation is different. The reverse shock propagates into the GRB ejecta for a long time and thus influences the afterglow emission during the first hours significantly (see numerical calculations in §4).

²Except for specific declarations, a quantity Q' with a prime is measured in the comoving frame of a certain region, while Q_\oplus with a subscript “ \oplus ” is measured in the observer’s frame, and the other Q is measured in the local medium’s rest frame. In addition, a subscript “ $i = 1, 2, 3, 4$ ” represents a quantity describing region “ i ”.

(ii) *The RSE model.* As suggested by Rees & Mészáros (1998), the mass distribution in the wide GRB ejecta associated with a distribution of bulk Lorentz factors reads

$$M_{\text{ej}}(> \Gamma_{\text{ej}}) \propto \Gamma_{\text{ej}}^{-s}. \quad (3)$$

Moreover, we assume that the Γ_{ej} -distribution in the GRB ejecta satisfies

$$\Gamma_{\text{ej}}(x) \propto x^{-1/b}, \quad (4)$$

where x is the displacement of the reverse shock propagating into the ejecta. We denote the Lorentz factor of the end of the ejecta (i.e., the minimum Lorentz factor) as $\Gamma_{\text{ej,min}}$, then the total displacement of the reverse shock when it crosses the ejecta could be estimated as $R_{\text{cross}}/2\Gamma_{\text{ej,min}}^2 \sim 10^{13} - 10^{14}$ cm. Under these assumptions, the associated injecting energy distributes with respect to x as $E_{\text{ej}} \propto x^{s/b}$, and the values of $n_4^{(\text{RSE})}$ and $\Gamma_4^{(\text{RSE})}$ are given by

$$n_4^{(\text{RSE})} = n'_{\text{ej}}(x) = \frac{dM_{\text{ej}}/dx}{4\pi R^2 \Gamma_{\text{ej}}(x) m_{\text{p}}}, \quad (5)$$

$$\Gamma_4^{(\text{RSE})} = \Gamma_{\text{ej}}(x), \quad (6)$$

where m_{p} is the proton rest mass.

2.2. Dynamic equations

Now, we describe the dynamic evolution of the system under the effect of two types of injecting flows that maintain a long-lasting reverse shock. The reverse shock transforms continuously the injecting energy into the internal energy of the reverse-shocked materials. Meanwhile, a part of fresh energy is further transformed to the kinetic energy ($E_{\text{K},2}$) of region 2 through the work done by region 3: $\delta W = 4\pi P'_3 R^2 dR$, where P'_3 is the pressure of region 3. Then, we have

$$\delta W = dE_{\text{K},2} = d[(\Gamma_2^2 - 1)M_{\text{sw}}c^2], \quad (7)$$

where M_{sw} is the rest mass of the swept-up medium and Γ_2 is the average bulk Lorentz factor of the shocked medium. Thus, the dynamic evolution of region 2 is described by (Dai 2004)

$$\frac{d\Gamma_2}{dR} = \frac{4\pi R^2 [P'_3/c^2 - (\Gamma_2^2 - 1)nm_{\text{p}}]}{2\Gamma_2 M_{\text{sw}}}, \quad (8)$$

where $dM_{\text{sw}}/dR = 4\pi R^2 nm_{\text{p}}$ is applied. To integrate the above equation, the pressure of region 3 should be calculated by

$$P'_3 = \frac{1}{3}(\Gamma'_{34} - 1)(4\Gamma'_{34} + 3)n'_4 m_{\text{re}} c^2, \quad (9)$$

where $\Gamma'_{34} = \Gamma_3\Gamma_4(1 - \beta_3\beta_4)$ is the Lorentz factor of region 3 measured in region 4 and β_i is the velocity in units of c , and m_{re} represents the electron and proton rest masses for the RWB and RSE models, respectively. The evolution of Γ_3 can be obtained from the equality of Lorentz factors of the two sides of the contact discontinuity surface, assuming that the shocked medium in region 2 satisfies the adiabatic self-similar solution of Blandford & McKee (1976)

$$\Gamma_3 = \Gamma_2\chi^{-1/2}. \quad (10)$$

To fix the self-similar variable χ , we use the following relationship,

$$P'_3 = \frac{4}{3}\Gamma_2^2 n_1 m_p c^2 \chi^{-17/12}. \quad (11)$$

Combining Eqs. 9, 10, and 11 to eliminate χ , we can solve Γ_3 and P'_3 as functions of Γ_2 and thus integrate Eq. 8. Simultaneously, the rest mass of region 3 is obtained from

$$\frac{dM_3}{dR} = 4\pi R^2 (\beta_4 - \beta_{\text{RS}}) \Gamma_4 n'_4 m_{\text{re}}, \quad (12)$$

where $\beta_{\text{RS}} = (\Gamma_3 n'_3 \beta_3 - \Gamma_4 n'_4 \beta_4) / (\Gamma_3 n'_3 - \Gamma_4 n'_4)$ is the velocity of the reverse shock.

When the reverse shock crosses the wind or GRB ejecta, the dynamic evolution of region 3 is described by Kobayashi & Sari (2000) and Kobayashi (2000). Then, the pressure of region 3 in Eq. 8 decreases significantly and thus is negligible. Meanwhile, the dynamic equation of region 2 returns to the form describing the standard afterglow model in Huang et al. (1999).

3. Electron distributions and emission mechanisms

After the dynamic evolution equations are given, the internal physics of the shocked regions in the RWB and RSE models can be considered as follows.

3.1. Electron energy distributions

As the forward and reverse shocks propagate, the bulk kinetic energies of the shells are gradually transformed into the internal energy of the shocked materials, the density of which is denoted by e'_i . This internal energy will be partly carried by the accelerated electrons and magnetic fields, the energy densities of which are fractions $\epsilon_{e,i}$ and $\epsilon_{B,i}$ of the total internal density, respectively. Through the shock acceleration, the electrons behind the forward/reverse shock will obtain an initial energy distribution $N'_{\text{ini},i}(\gamma'_i) \propto \gamma'^{-p}_i$ with the

minimum Lorentz factor $\gamma'_{m,i} = \lambda_i[(p-2)/(p-1)]\epsilon_{e,i}(\tilde{\Gamma}_i - 1)$ and the maximum Lorentz factor $\gamma'_{\max,i} \approx 10^8[B'_i(1+Y_i)]^{-1/2}$, where $\lambda_2 = m_p/m_e$, $\lambda_3 = m_{re}/m_e$, $\tilde{\Gamma}_2 = \Gamma_2$, $\tilde{\Gamma}_3 = \Gamma'_{34}$, and B'_i is the magnetic field strength. The occurrence of the Compton parameter Y_i is induced by the IC cooling effect. By considering the cooling effect of the synchrotron and IC radiation, we can get the actual electron energy distributions (Huang et al. 2000):
for $\gamma'_{c,i} \leq \gamma'_{m,i}$,

$$N'_i(\gamma'_i) \propto \begin{cases} \gamma'^{-2}_i & \text{if } \gamma'_{c,i} \leq \gamma'_i \leq \gamma'_{m,i}, \\ \gamma'^{-p-1}_i & \text{if } \gamma'_{m,i} < \gamma'_i \leq \gamma'_{\max,i}; \end{cases} \quad (13)$$

and for $\gamma'_{c,i} > \gamma'_{m,i}$,

$$N'_i(\gamma'_i) \propto \begin{cases} \gamma'^{-p}_i & \text{if } \gamma'_{m,i} \leq \gamma'_i \leq \gamma'_{c,i}, \\ \gamma'^{-p-1}_i & \text{if } \gamma'_{c,i} < \gamma'_i \leq \gamma'_{\max,i} \end{cases} \quad (14)$$

where the cooling Lorentz factor $\gamma'_{c,i}$ is defined by the cooling timescale that equals to dynamic expansion timescale of the system, that is,

$$\gamma'_{c,i} = \frac{6\pi m_e c}{(1+Y_i)\sigma_T \Gamma_i B'^2_i t_{\oplus}} \quad (15)$$

with σ_T being the Thomson scattering cross section. In addition, the self-absorption of the synchrotron photons is ignored in Eqs. 13 and 14 for the high-energy emission that we are interested in. Following Sari & Esin (2001), the Compton parameter Y_i in Eq. 15, defined as the ratio of the IC (including SSC and CIC) luminosity to the synchrotron luminosity of electrons, is estimated by

$$Y_2 \equiv \frac{L'_{IC,2}}{L'_{syn,2}} = \frac{U'_{syn,2} + \frac{1}{2}U'_{syn,3}}{U'_{B,2}}, \quad (16)$$

$$Y_3 \equiv \frac{L'_{IC,3}}{L'_{syn,3}} = \frac{U'_{syn,3} + \frac{1}{2}U'_{syn,2}}{U'_{B,3}}, \quad (17)$$

where $U'_{syn,i} = \eta_i \epsilon_{e,i} e'_i / (1+Y_i)$ and $U'_{B,i} = \epsilon_{B,i} e'_i$ are the energy densities of synchrotron seed photons and magnetic field, respectively. The radiation efficiency η_i reads

$$\eta_i = \begin{cases} 1, & \text{for } \gamma'_{c,i} \leq \gamma'_{m,i}, \\ (\gamma'_{c,i}/\gamma'_{m,i})^{2-p}, & \text{for } \gamma'_{c,i} > \gamma'_{m,i}. \end{cases} \quad (18)$$

A factor of $\frac{1}{2}$ in Eqs. 16 and 17 occurs, because only about one-half of seed photons from one shocked region will diffuse into the other one for the CIC process. In two extreme situations, Eqs. 16 and 17 can be simplified as

i) for $U'_{syn,3} \gg U'_{syn,2}$,

$$Y_2 = \eta_3 \frac{\epsilon_{e,3} e'_3}{2\epsilon_{B,2} e'_2} (1+Y_3)^{-1}, \quad Y_3 = \eta_3 \frac{\epsilon_{e,3}}{\epsilon_{B,3}} (1+Y_3)^{-1}; \quad (19)$$

ii) for $U'_{\text{syn},3} \ll U'_{\text{syn},2}$,

$$Y_2 = \eta_2 \frac{\epsilon_{e,2}}{\epsilon_{B,2}} (1 + Y_2)^{-1}, \quad Y_3 = \eta_2 \frac{\epsilon_{e,2} e'_2}{2\epsilon_{B,3} e'_3} (1 + Y_2)^{-1}. \quad (20)$$

3.2. SSC and CIC emission

Once the electron distributions are known, the synchrotron emissivity of electrons in region i at frequency ν' is calculated directly by (Rybicki & Lightman 1979)

$$\varepsilon_i^{\text{syn}}(\nu') = \frac{\sqrt{3} q_e^3 B'_i}{m_e c^2} \int d\gamma'_i N'_i(\gamma'_i) \mathcal{F}\left(\frac{\nu'}{\nu'_c}\right), \quad (21)$$

where q_e is the electron charge, $\nu'_c = 3\gamma_i^2 q_e B'_i / (4\pi m_e c)$, $\mathcal{F}(u) = u \int_u^\infty K_{5/3}(k) dk$, and $K_{5/3}(k)$ is the Bessel function.

Accompanying with the synchrotron radiation, the electrons also lose their energy through upscattering the synchrotron seed photons. As usual, the first-order IC scattering is considered and the higher-order processes are neglected. According to Blumenthal & Gould (1970), when the Klein-Nishina suppression is considered, the IC emissivity (at frequency ν') of electrons in region i upscattering seed photons from region j is calculated by ($i = j$ for SSC and $i \neq j$ for CIC)

$$\varepsilon_i^{\text{IC}(j)}(\nu') = 3\sigma_T \int d\gamma'_i N'_i(\gamma'_i) \int d\nu_j^\dagger \frac{\nu' f_j^\dagger}{4\gamma_i'^2 \nu_j^{\dagger 2}} g(x, y), \quad (22)$$

where $g(x, y) = 2y \ln y + (1 + 2y)(1 - y) + \frac{1}{2} \frac{x^2 y^2}{1 + xy} (1 - y)$ with $x = 4\gamma_i' h\nu_j^\dagger / m_e c^2$, $y = h\nu' / [x(\gamma_i' m_e c^2 - h\nu')]$. ν_j^\dagger and f_j^\dagger are the frequency and the corresponding flux density of the incident photons from region j , respectively, which are measured in the comoving frame of region i .

The observed synchrotron and IC flux densities at frequency ν_\oplus from region i are given respectively by (Huang et al. 2000)

$$F_{\oplus, \nu_\oplus, i}^{\text{syn}}(t_\oplus) = \int_0^\pi d\theta V'_i \frac{\sin \theta}{2} \frac{\varepsilon_i^{\text{syn}}(\mathcal{D}_i \nu_\oplus)}{4\pi D_L^2 \mathcal{D}_i^3}, \quad (23)$$

$$F_{\oplus, \nu_\oplus, i}^{\text{IC}(j)}(t_\oplus) = \int_0^\pi d\theta V'_i \frac{\sin \theta}{2} \frac{\varepsilon_i^{\text{IC}(j)}(\mathcal{D}_i \nu_\oplus)}{4\pi D_L^2 \mathcal{D}_i^3}, \quad (24)$$

where D_L is the luminosity distance and $\mathcal{D}_i = \Gamma_i(1 - \beta_i \cos \theta)$ is the Doppler factor (here θ is the angle between the moving direction of the emitting material and the line of sight).

Herein, we assume the viewing angle $\theta_{\text{obs}} = 0$. The volumes V'_i of the shocked regions in Eqs. 23 and 24 are functions of θ since the integrations are performed over the equal-arrival surface. In addition, the jet correction should be considered if the GRB ejecta is collimated.

4. Numerical Results

4.1. Dynamic evolution

For the RWB and RSE models, we first calculate the dynamic evolution with radius larger than the deceleration radius that is taken to be $\sim 10^{16}$ cm. For the RWB model, as in Yu & Dai (2007), the isotropic wind luminosity is $L_w = 4 \times 10^{47} B_{14}^2$ erg s $^{-1}$, the wind duration $T_w = 5 \times 10^4 B_{14}^{-2}$ s, and the bulk Lorentz factor of the wind $\Gamma_w = 10^4$, where B_{14} is the magnetic field strength of the central magnetar in unit of 10^{14} G. Here, we take $B_{14} = 4$ for a typical magnetar. Thus the total energy of the wind is $E_w = 2.0 \times 10^{52}$ erg. However, the isotropic kinetic energy of the previous GRB ejecta is relative small, $E_{\text{ej}}^{\text{RWB}} = 10^{51}$ erg. For consistency, we assume that, in the RSE model, the isotropic kinetic energy carried by the wide GRB ejecta is $E_{\text{ej}}^{\text{RSE}} = 2.1 \times 10^{52}$ erg, and the distribution-related parameters are $\Gamma_{\text{ej,min}} = 30$, $\Gamma_{\text{ej,max}} = 500$, and $s = b = 1.5$. In addition, the number density of the ambient interstellar medium is $n_1 = 1$ cm $^{-3}$ in both cases.

The dotted lines in Fig. 2 represent the dynamic evolution of the shells for a certain energy (i.e., without energy injection), and the solid lines show the energy injection case. We can see clearly from this figure that the energy ($\propto \Gamma_2^2$) of the shocked medium increases gradually until the energy injection is over. As analyzed in Yu & Dai (2007), the final energy carried by region 2 is a fraction $\sim 67\%$ of the total injecting energy for the RWB model versus $\sim 90\%$ for the RSE model. Meanwhile, the other fraction of the injecting energy ($\sim 33\%$ and $\sim 10\%$ for the RWB and RSE models, respectively) should be shared by the reverse-shocked material. In addition, we know that the reverse shock is relativistic in the RWB model, but Newtonian or trans-relativistic in the RSE model, according to an estimation of the Lorentz factor of region 3 relative to region 4 from

$$\Gamma'_{34} \approx \frac{1}{2} \left(\frac{\Gamma_3}{\Gamma_4} + \frac{\Gamma_4}{\Gamma_3} \right) \quad (25)$$

with the values of Γ_3 as shown in Fig. 2. This difference between the reverse shocks of the two models is just the reason why the reverse shock in the RWB model can share more injecting energy than the one in the RSE model.

4.2. Spectra and light curves

To calculate the emission of shocked materials, we take the microphysical parameters $p = 2.3$, $\epsilon_B = 0.01$, and $\epsilon_e = \sqrt{\epsilon_B}$ for the baryon-dominated region (Medvedev 2006) and $\epsilon_e = 1 - \epsilon_B$ for the lepton-dominated region. The luminosity distance of a GRB is taken to be $D_L = 1$ Gpc, corresponding to a redshift of 0.2.

Figure 3 shows the light curves of a RWB. From this figure, we obtain the following results. First, the shallow decay phase of an X-ray (keV) afterglow is produced during the early hours (left upper panel), which is mildly dominated by the reverse shock emission (for a detailed discussion see Yu & Dai 2007). The synchrotron radiation is a dominative mechanism in this band. Second, an obvious hump accompanying with the X-ray plateau occurs in a high-energy (MeV & GeV) afterglow, which is dominated by the IC, especially SSC, emission from the reverse-shocked wind. Finally, a comparison of light curves in different bands (right lower panel) shows that the high-energy (especially GeV) emission flux is mildly or even significantly higher than the one in X-ray band. This feature is also implied obviously from the spectra as shown in Fig. 4. The peak flux of the IC emission at ~ 1 GeV is about one order of magnitude higher than the synchrotron peak at ~ 10 eV. Above sub-MeV, the IC component is dominative. Moreover, in all bands, the emission from the reverse-shocked wind at 1000 s is more important than the one from the forward-shocked medium.

The results for the RSE model are shown in Figs. 5 and 6. From these two figures, we find that, first, the X-ray shallow decay phase during the early hours is also produced in this model as shown in left upper panel of Fig. 5, which is dominated by the forward shock. Second, the high-energy afterglow light curves also have a flattening segment. However, differing from the RWB model, the contribution to the high-energy plateau from the IC emission plays a role only in GeV band, whereas the MeV emission is totally contributed by the synchrotron mechanism during the total afterglow phase. This result arises from the relative weakness of the IC component in the RSE model as shown in Fig. 6. Therefore, the flux in MeV or GeV band is lower or slightly higher than the X-ray flux as shown in right lower panel of Fig. 5. In addition, Figure 6 shows that the contribution of the emission from the reverse-shocked ejecta is negligible in all bands for the parameters that we adopt.

In conclusion, we obtain very different high-energy afterglow light curves from the RWB and RSE models with the same amount of injecting energy that gives rise to similar X-ray afterglows. The RWB model predicts more significant (about one order of magnitude stronger) high-energy emission than the RSE model. The reasons for this difference are that the reverse shock in the RWB model is relativistic and that the energy of the reverse shock is almost totally carried by electrons. The former reason enables the reverse shock to share more (i.e., 33% vs 10%) injecting energy as discussed in Sect. 4.1, and the latter

reason dramatically increases the emission efficiency of the reverse-shocked material through the enhanced IC emission. Therefore, a higher fraction of injecting energy can be radiated from the shocked regions in the RWB model. In the baryonic-component-dominated model, however, this significant enhanced IC component doesn't happen even if the emission flux from the reverse shock exceeds the one of the forward shock under some extreme conditions, because most of the injecting energy in both shocked regions is locked in the baryons whose emission is weak. Therefore, we argue that the difference of the high-energy emission between the RWB and RSE models is essentially due to the physical distinction between the two types of energy injection. Thus, reasonable variations of the parameters for the models should not change our results significantly.

5. Summary and discussion

The discovered shallow decay phase of GRB X-ray afterglows suggests long-lasting energy injection into relativistic blast waves. The injecting energy flow is likely to be dominated by baryons or leptons. In this paper, we have provided a unified description for the dynamics and radiation in two representative models (i.e., the RSE and RWB models). As a result, the flattening segment of X-ray afterglow light curves can be produced by two types of energy injection through doing work to the shocked medium and producing a long-lasting reverse shock. Furthermore, we calculated the simultaneous high-energy emission that is due to synchrotron and, especially, IC scattering (including SSC and CIC processes) in the shocked materials. Our calculations show that, during the shallow decay phase of X-ray afterglows, there is a plateau (even a hump) in the high-energy light curves in the RSE and RWB models. As argued by Wei & Fan (2007), we suggested that the plateau/hump might account for the delayed high-energy emission of some bursts such as GRB 940217.

We also found that the high-energy emission predicted by the two models has different observable features, e.g., morphology of the light curves, the spectra, and the ratio of the flux in \sim GeV band to the flux in X-ray. It is easy to understand that more significant high-energy emission is predicted by the RWB model, because more injecting energy in this model is carried by electrons and thus the IC scattering is enhanced significantly. This difference in high-energy emission of the two models could be tested in the upcoming GLAST era. The fluence threshold of the LAT instrument of GLAST, as proposed by Zhang & Mészáros (2001b) and Gou & Mészáros (2007), is estimated by $F_{\text{thr}} \sim E\Phi_0 T(t/T)^{1/2}$ for a long-time observation, where E is the average energy of an interesting band, Φ_0 the flux sensitivity, T the effective observation time, and t the integration time. However, for a short-time observation, the fluence threshold is instead calculated by $F_{\text{thr}} = 5E/A_{\text{eff}}$ with the

assumption that at least 5 photons are collected by an effective area A_{eff} of the instrument. Because $\Phi_0 \sim 4 \times 10^9 \text{ ph s}^{-1} \text{ cm}^{-2}$ above 100 MeV for the GLAST LAT, $T = \eta \times 1 \text{ yr}$ ($\eta \sim 0.5$ is the observation efficiency due to the occultation by the earth), and $A_{\text{eff}} = 6000 \text{ cm}^2$, we obtain the fluence threshold at 400 MeV,

$$F_{\text{thr}} = \begin{cases} 5.3 \times 10^{-7} \text{ erg cm}^{-2}, & t \leq 2.43 \times 10^4 \text{ s}, \\ 3.4 \times 10^{-9} t^{1/2} \text{ erg cm}^{-2}, & t > 2.43 \times 10^4 \text{ s}, \end{cases} \quad (26)$$

which is shown in Fig. 7 by the dotted line. Figure 7 shows the observability of high-energy emission in the RWB and RSE models. It can be seen from this figure that for the same amount of injecting energy, the partial fluence of the high-energy emission for the RWB model is about an order of magnitude higher than that for the RSE model (where the partial fluence is defined by a product of flux and time as in Zhang & Mészáros 2001b). So, the high-energy emission in the RWB model is easier to detect by the LAT instrument on GLAST.

Acknowledgements

This work is supported by the National Natural Science Foundation of China (grant no. 10221001 and 10640420144). YWY is also supported by the Visiting PhD Candidate Foundation of Nanjing University and the National Natural Science Foundation of China (grant no.10603002).

REFERENCES

- Blandford, R. D., & McKee, C. F. 1976, *Phys. Fluids.*, 19, 1130
- Blumenthal, G. R., & Gould, R. J. 1970, *Rev. Mod. Phys.*, 42, 237
- Coroniti, F. V. 1990, *ApJ*, 349, 538
- Dai, Z. G. 2004, *ApJ*, 606, 1000
- Dai, Z. G., & Lu, T. 1998a, *A&A*, 333, L87
- Dai, Z. G., & Lu, T. 1998b, *Phys. Rev. Lett.*, 81, 4301
- de Pasquale, M., et al. 2006, *MNRAS*, 365, 1031
- de Pasquale, M., et al. 2007, accepted by *MNRAS*, arXiv:astro-ph/0703447

- Fan, Y. Z., & Xu, D. 2006, MNRAS, 372, L19
- Fan, Y. Z., Piran, T., Narayan, R., & Wei, D. M., 2007, submitted to MNRAS, arXiv:0704.2063
- Genet, F., Daigne, F., & Mochkovitch, R. 2007, arXiv:astro-ph/0701204
- Gou, L. J., & Mészáros, P. 2007, accepted by ApJ, arXiv:0705.1545
- Granot, J., & Kumar, P., 2006, MNRAS, 366, L13
- Huang, Y. F., Dai, Z. G., & Lu, T. 1999, MNRAS, 309, 513
- Huang, Y. F., Gou, L. J., Dai, Z. G. & Lu, T. 2000, ApJ, 543, 90
- Kirk, J. G., & Skjæraasen, O. 2003, ApJ, 591, 366
- Kobayashi, S. 2000, ApJ, 545, 807
- Kobayashi, S., & Sari, R. 2000, ApJ, 542, 819
- Liang, E. W., Zhang, B. B., & Zhang, B. 2007, submitted to ApJ, arXiv:0705.1373
- Liu, X. W., Wu, W. F., Zou, Y. C., & Lu, T. 2007, to be submitted
- Medvedev, M. V. 2006, ApJ, 651, L9
- Mészáros, P., & Rees, M. J. 1997, ApJ, 476, 232
- Michel, F. C. 1994, ApJ, 431, 397
- Nousek, J. A., et al. 2006, ApJ, 642, 389
- O’Brien, P. T., et al. 2006, ApJ, 647, 1213
- Panaitescu, A., Mészáros, P., & Rees, M. J. 1998, ApJ, 503, 314
- Rees, M. J., & Mészáros, P. 1998, ApJ, 496, L1
- Ritz, S. 2007, a review talk in the First GLAST Symposium (5 February 2007)
- Rybicki, G. B., & Lightman, A. P. 1979, Radiative Processes in Astrophysics (New York: Wiley)
- Sari, R., & Esin, A. A. 2001, ApJ, 548, 787
- Sari, R., Piran, T., & Narayan, R. 1998, ApJ, 497, L17

- Sari, R., & Mészáros, P. 2000, ApJ, 535, L33
- Sollerman, J., et al. 2007, A&A, 466, 839
- Uhm, Z. L., & Beloborodov, A. M. 2007, accepted by ApJ Letters, arXiv:astro-ph/0701205
- Wang, W., & Dai, Z. G. 2001, Chin. Phys. Lett., 18, 1153
- Wang, X. Y., Dai, Z. G., & Lu, T., 2001, ApJ, 556, 1010
- Wei, D. M., & Fan, Y. Z. 2007, ChJAA, in press, arXiv:astro-ph/0702106
- Willingale, R., et al. 2007, ApJ, 662, 1093
- Yu, Y. W., & Dai, Z. G. 2007, accepted by A&A, arXiv:0705.1108
- Zhang, B., et al. 2006, ApJ, 642, 354
- Zhang, B., & Mészáros, P. 2001a, ApJ, 552, L35
- Zhang, B., & Mészáros, P. 2001b, ApJ, 559, 110

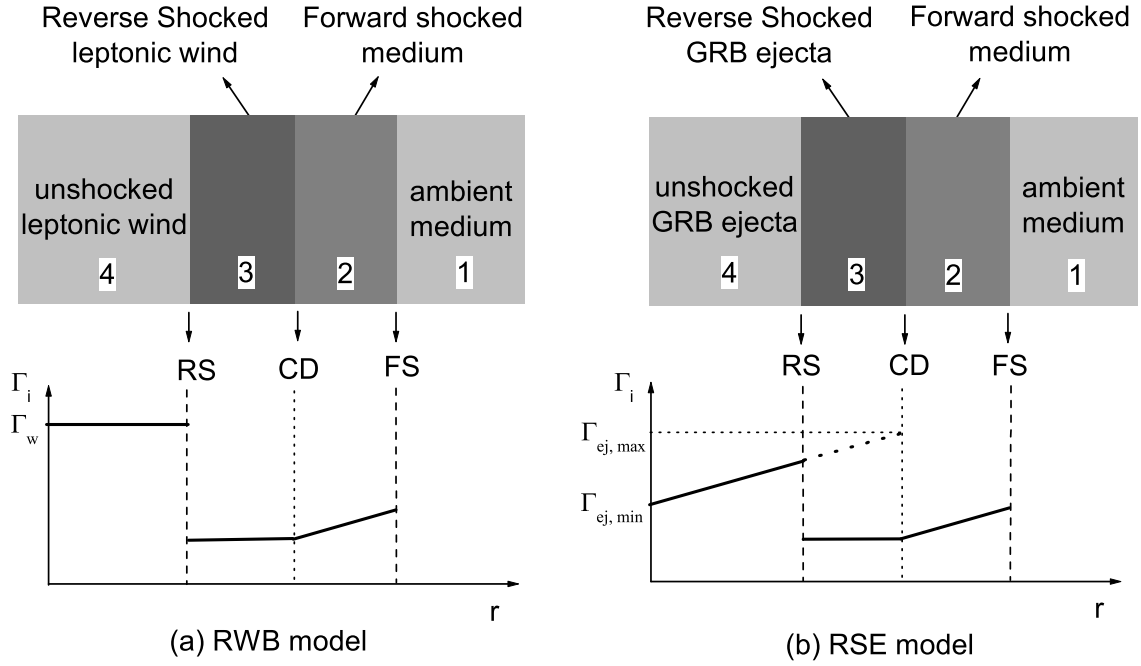


Fig. 1.— Illustrations of four regions divided by the forward and reverse shocks in the RWB (left) and RSE (right) models, and the corresponding distributions of Lorentz factors (not scaled).

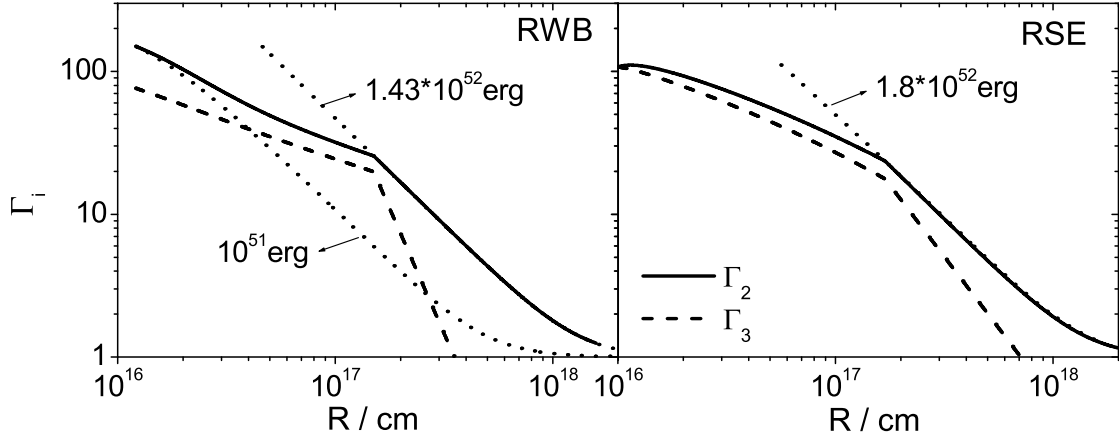


Fig. 2.— The evolution of the Lorentz factors of regions 2 and 3 as the expansion of the shells for the RWB (left) and RSE (right) models. A dotted line represents the dynamic evolution of the shell with a fixed amount of energy as labeled.

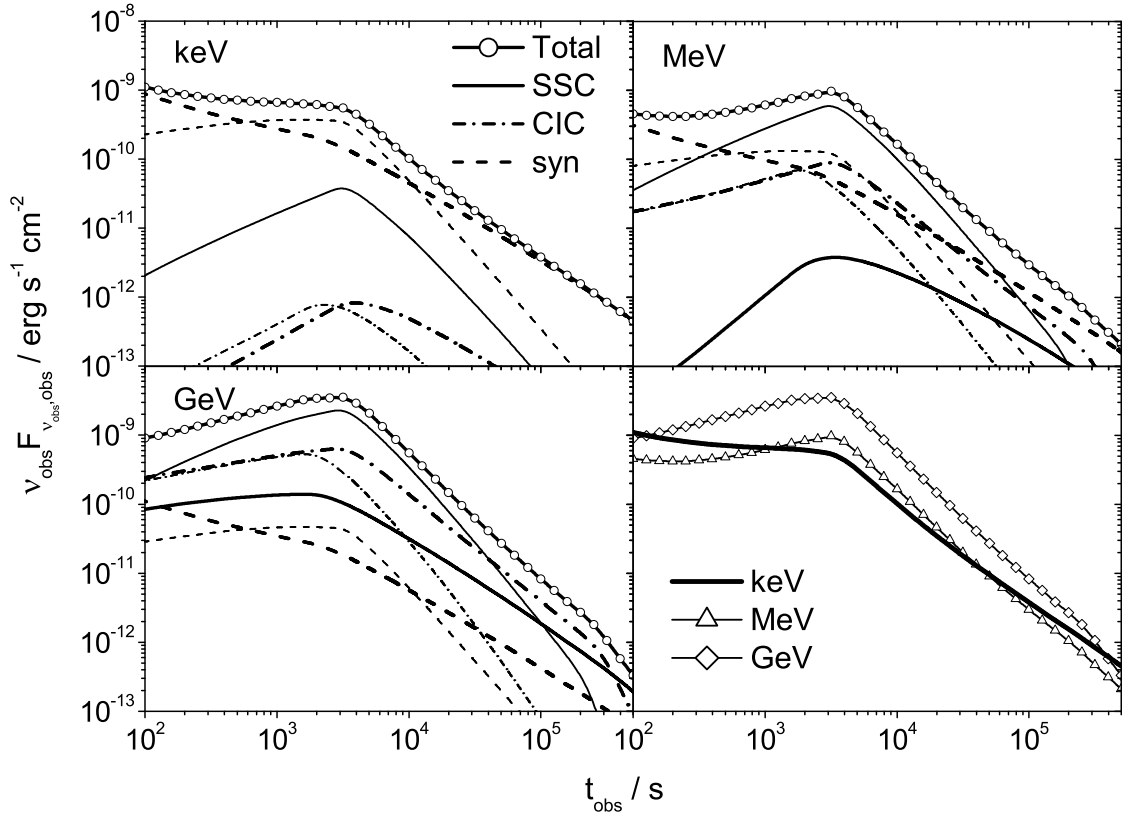


Fig. 3.— Light curves in X-ray (keV) and high energy gamma-ray (MeV, GeV) bands for the RWB model. The emission from the forward-shocked medium is represented by thick lines, while the reverse shock corresponds to thin lines. The solid, dash-dotted, and dashed lines are due to SSC, CIC, and synchrotron processes, respectively.

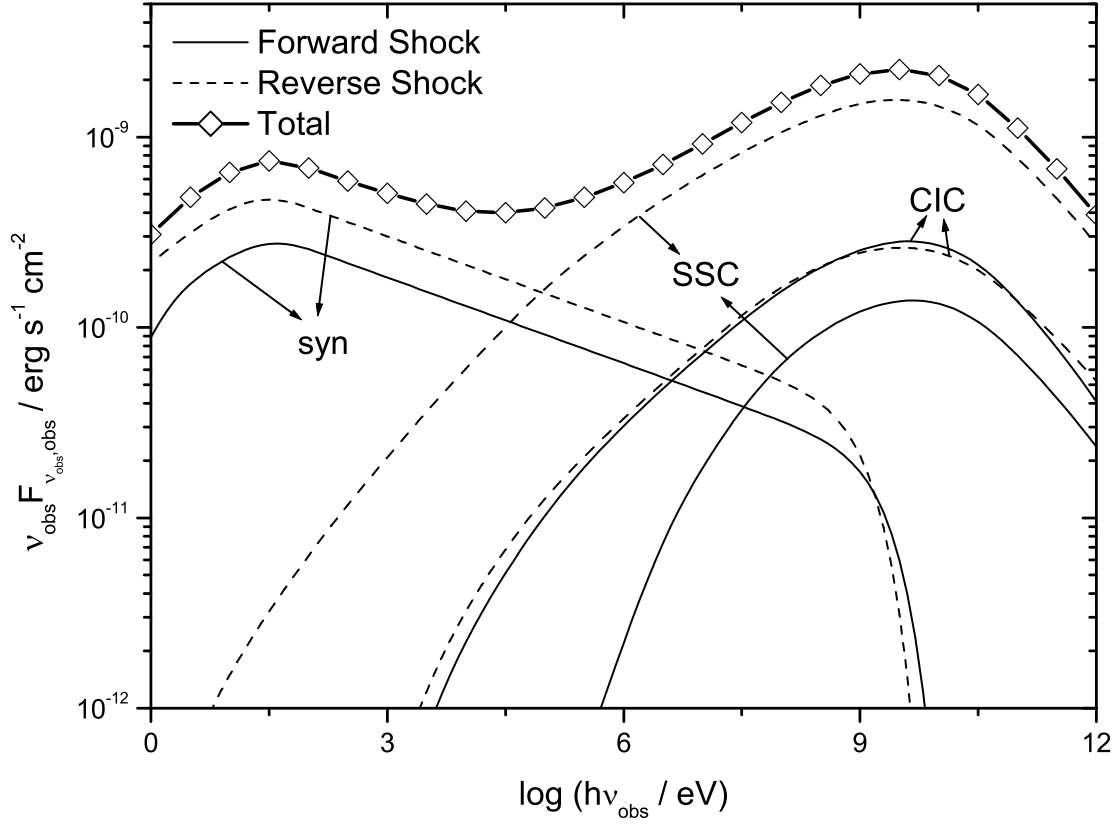


Fig. 4.— The synchrotron and IC spectra at 1000 s for the RWB model. The solid lines represent the emission contributed by the forward-shocked medium, while the dotted lines correspond to the reverse-shocked wind.

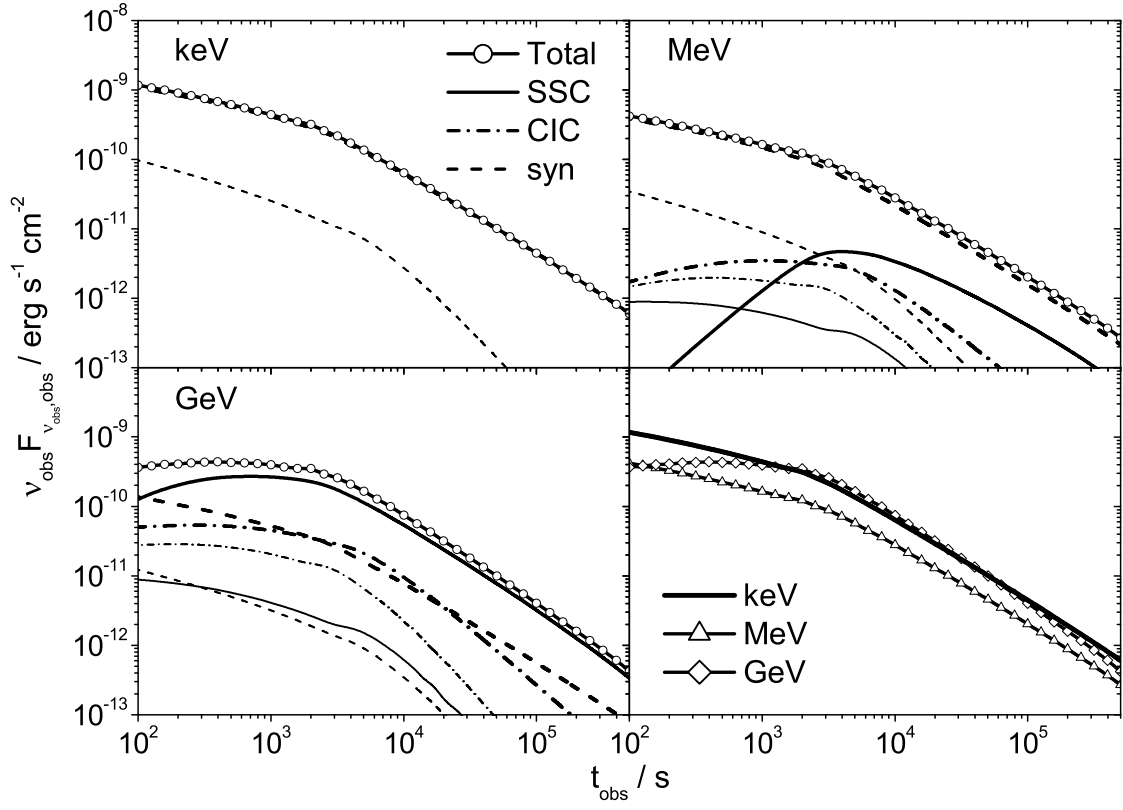


Fig. 5.— Same as in Fig. 3 but for the RSE model.

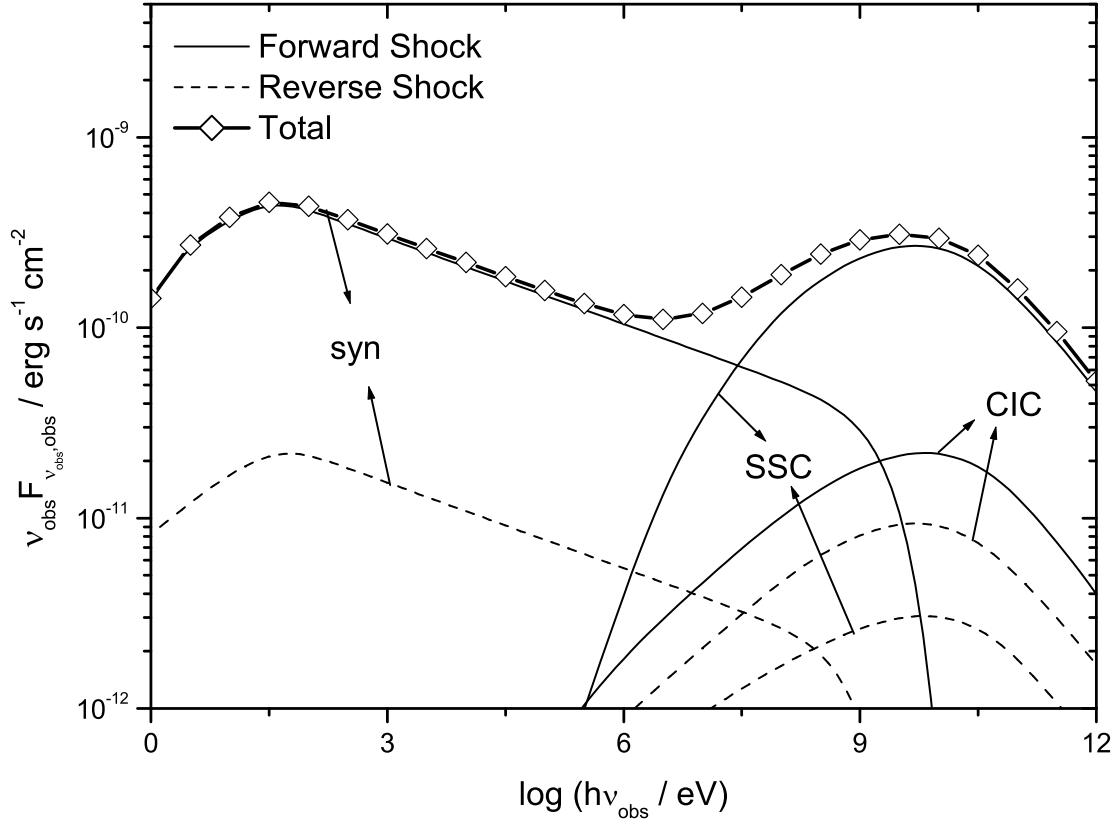


Fig. 6.— Same as in Fig. 4 but for the RSE model.

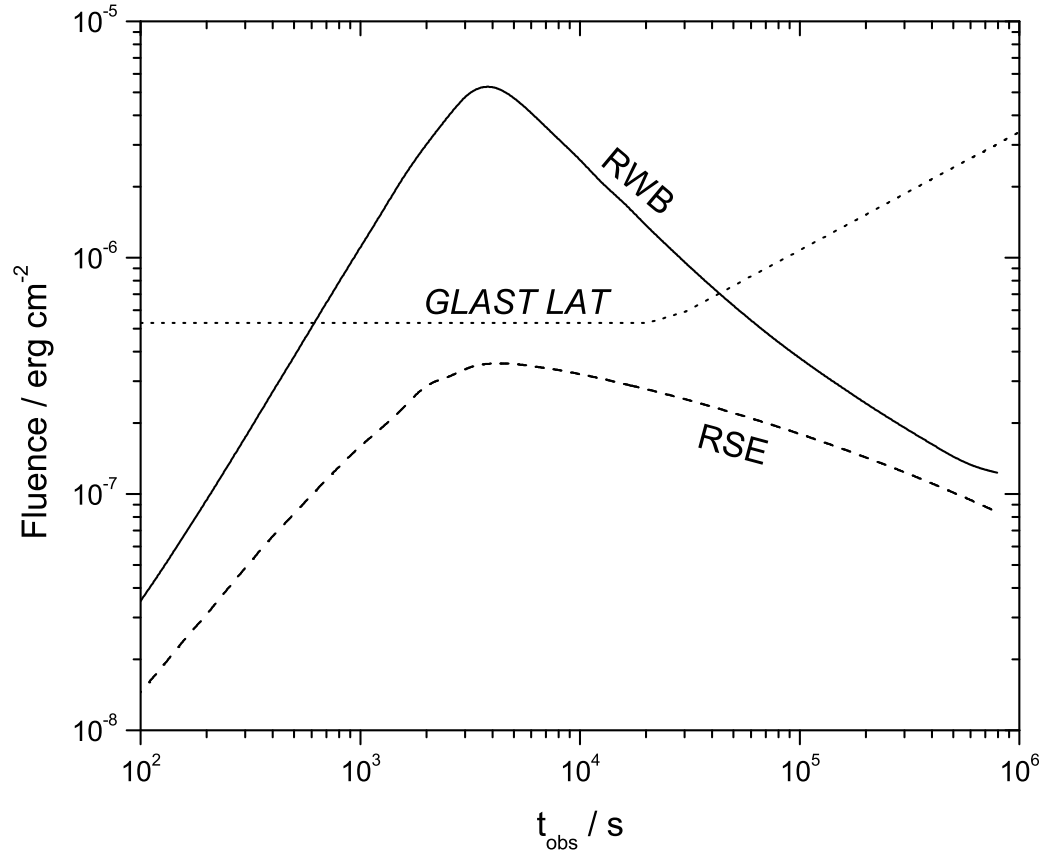


Fig. 7.— The partial fluence curves at 400 MeV for the RWB and RSE models. The dotted line represents the sensitivity of the GLAST LAT.